

## Recent SAXS Progress at NSRRC

U. Jeng\*, C.-H. Hsu, Y.-S. Sun, Y.-H. Lai, W.-T. Chung, H.-S. Sheu, H.-Y. Lee, Y.-F. Song, and K. S. Liang

*National Synchrotron Radiation Research Center, Hsinchu 300, Taiwan*

T.-L. Lin

*Department of Engineering and System Science, National Tsing Hua University, Hsinchu 300, Taiwan*

*Received August 11, 2005; Revised October 25, 2005*

**Abstract:** We review the recent SAXS activity on the 1.5-GeV electron storage ring at the National Synchrotron Radiation Research Center (NSRRC). Typical measurements featuring in grazing incident SAXS for soft materials are illustrated. Complex measurements using simultaneous SAXS/DSC and SAXS/WAXS for the correlations between the crystallization and mesoscale ordering in a polymer blend and a polypeptide-*block*-polypseudorotaxane diblock copolymer are presented. We also introduce a dedicated SAXS beamline which is planned at NSRRC.

**Keywords:** NSRRC, SAXS activity, beamline.

### Introduction

Small angle X-ray scattering (SAXS), a scattering tool of molecular spatial resolution and high penetration power, provides a non-destructive scattering tool in structure characterization for surfaces, interfaces, as well as bulks, and is an decent complimentary technique to direct imaging tools such as TEM, SEM, and AFM in nanostructure research. Capable of probing structural information (electron density fluctuations) in a wide range of length scale spanning from sub-nanometer to sub-micron, SAXS has been often used in many fields where nanostructures and/or mesomorphous structure take a decisive role in determining phases, functions, and/or performances of devices.

With the sacrifice of atomic resolution, SAXS probes mean electron density fluctuations in matter. This feature grants the convenience of using a mean-filed approximation in describing electron distribution of nano- to meso-scale characteristic lengths inside materials. X-ray scattering by the density fluctuations of these length scales features mainly in a low scattering angle field, and can be conveniently described by  $I(q) = \left| \int \rho(r) e^{-iq \cdot r} d^3r \right|^2$ , with the wavevector transfer  $q = 4\pi \sin(\theta/2)/\lambda$  defined by the scattering angle  $\theta$  and wavelength  $\lambda$  of the photons. Studying the scattering profile  $I(q)$  measured, one can possibly retrieve the density distribution (or fluctuations) function  $\rho(r)$  of systems of little or no crystalline structures.<sup>1</sup>

The merits of SAXS in structural characterization have been recognized by many research groups in Taiwan.

Around five SAXS instruments equipped with in-house X-ray sources have been installed successively in recent years, and have produced fruitful results in the fields of, for instances, colloids, polymers, as well as alloys. Nevertheless, with limited flux ( $\sim 10^6$  photons/s) and fixed energy (mainly 8 KeV) of the in-house X-ray source, many advanced researches were frustrated. On the other hand, with the wiggler beamline and the superconducting-wavelength-shifter beamline at the NSRRC, we have high-flux photon sources ( $>10^{11}$  photons/s) more than five orders of magnitude higher than common in-house X-ray sources, with a wide energy range of 5-35 KeV. The photon sources have opened new SAXS research fields at the NSRRC, including time-resolved structural transitions, low scattering contrast systems such as protein folding dynamics or polymer morphology in solutions, and anomalous SAXS (ASAXS) for multiphase structures, like core-shell bimetallic nanoparticles in quantum dots or catalyst applications.<sup>2</sup> Below, we review the recent SAXS activity at the NSRRC, and introduce a dedicated SAXS beamline at the NSRRC in the near future.

### SAXS Activity at BL17B

Unconventionally, SAXS at the NSRRC started from the grazing incident SAXS (GISAXS) for thin film structures. In the earlier days, lacking of a dedicated beamline and instrument, SAXS measurements were conducted on a temporary setup modified from an 8-circle diffractometer at the wiggler beamline BL17B by Hsu *et al.*<sup>3</sup> The photons (5-14 KeV) were monochromated by a double crystal monochromator (DCM) of Si(111) and collimated by two sets of slits,

\*Corresponding Author. E-mail: usjeng@nsrrc.org.tw

generally set at  $0.4 \times 0.4$  and  $0.4 \times 0.6$  mm<sup>2</sup>, separated by one meter. The setup resulted in a photon flux of  $\sim 10^9$  photons/s at the sample position. With all the conveniences inherited from the mechanical freedoms of the 8-circle diffractometer, the setup was especially versatile in positioning and aligning thin-film samples for GISAXS. A NaI scintillation counter and a 50 mm position-sensitive linear detector located  $\sim 1$  m from the sample position, were used for reflectivity scan and GISAXS, respectively. The GISAXS setup usually allowed an angular resolution of  $0.028$  and  $0.006^\circ$ , or  $0.004$  and  $0.001 \text{ \AA}^{-1}$  in the  $q$ -space, in the vertical and horizontal directions, respectively. Between the sample and detector, the scattering path was evacuated through a 120 mm dia. PVC plastic pipe, with a 30 mm dia. entrance and a  $100 \times 100$  mm<sup>2</sup> squared exit sealed by thin Kapton films. Sitting inside the PVC pipe and in front of the exit window was the beamstop of a 4 mm dia. Pb-alloy disk attached to a stick of the same material, which could be positioned together with the PVC pipe that held on the 8-circle diffractometer. The lollipop shape of beamstop could block the direct beam as well as the strong specular beam from the detectors in GISAXS measurements. The transmis-

sion could be measured by moving the beamstop away (swinging the diffractometer arm horizontally), and exposed the detector to the attenuated direct beam for the intensity ratio (namely transmission) of the intensities collected with and without sample, respectively. The 50 mm linear detector could scan the scattering profile in the direction perpendicular to the linear axis of the detector for mapping out a two-dimensional scattering pattern (see Figure 1(a)).

Despite the simple setup, yet many thin film structures were studied. Figure 1 shows the GISAXS result for a low- $k$  dielectric silica xerogel film of  $\sim 6,000 \text{ \AA}$  thick, which was processed directly on a Si wafer. With the GISAXS geometry, we could obtain the internal structure of the undetachable porous film, including the pore shape, size, and averaged inter-pore spacing. Scanning the linear detector in the direction perpendicular to the sample plane, the degree of anisotropy of the film structure parallel and normal to the interface could be revealed.<sup>4</sup>

The positive result of GISAXS for the xerogel films triggered a series of GISAXS study, including lipid membranes,<sup>5</sup> lipid monolayers,<sup>6</sup> and monolayers of quantum dots. Figure 2 shows the X-ray reflectivity and GISAXS data for a

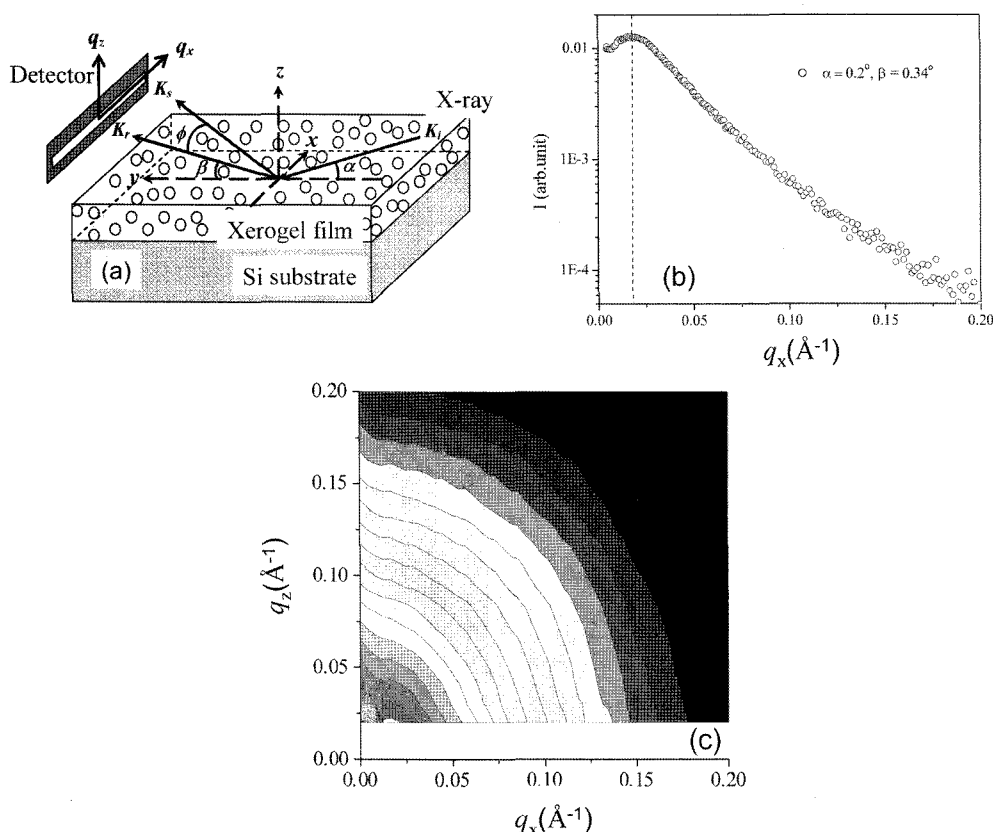


**Figure 1.** (a) A schematic of the GISAXS geometry. (b) The corresponding GISAXS data of the xerogel/Si sample collected at incident angle of  $\alpha=0.2^\circ$  and an exit angle  $\beta=0.34^\circ$ , with the linear detector along the  $q_x$  direction. The dashed line marks  $q_x=0.0175 \text{ \AA}^{-1}$  for the interference peak position, which corresponds to a mean pore spacing of  $\sim 400 \text{ \AA}$ . (c) A contour map of the asymmetrical GISAXS pattern of the xerogel film collected at  $\alpha=0.25^\circ$ , with the intensity decreases monotonically after  $q_x>0.0175 \text{ \AA}^{-1}$ .

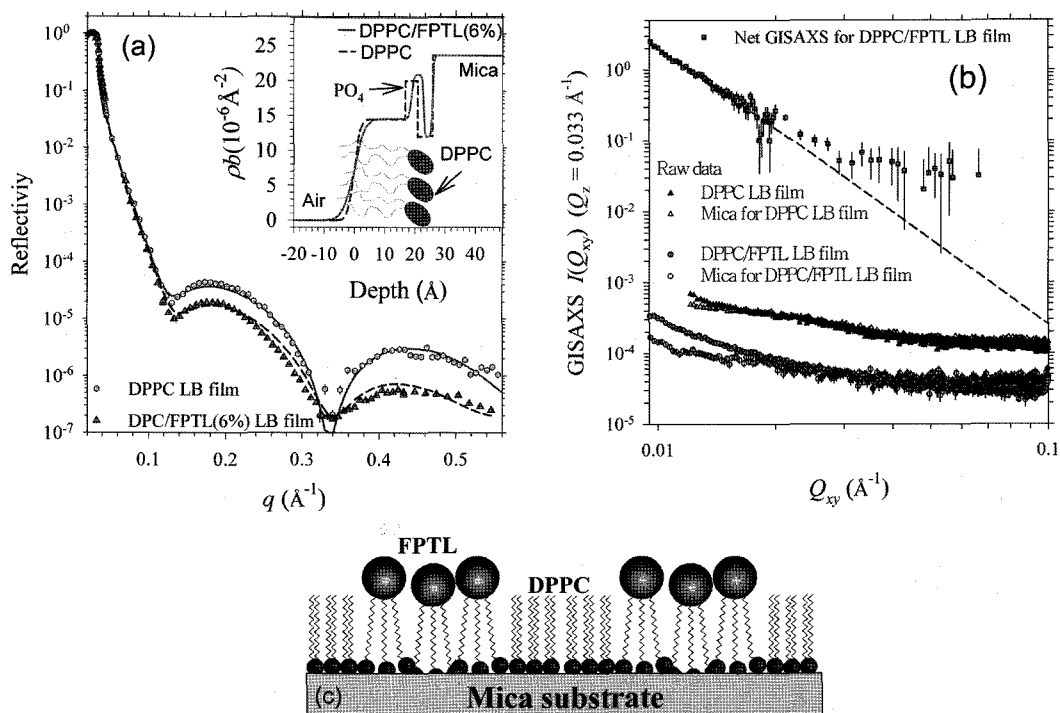


**Figure 2.** (a) Reflectivity data for the pure DPPC and DPPC/FPTL mixed Langmuir-Blodgett (LB) films. The data were fitted (solid and dashed curves) using the scattering-length-density profiles shown in the inset, respectively. (b) The grazing incidence SAXS for the DPPC/FPTL (solid circles) LB film on mica, the mica substrate, and the DPPC LB film. The net GISAXS data (squares) for the DPPC/FPTL film, with the scattering from mica subtracted, are rescaled and fitted (dashed curve) with a Debye-Buche model.  $Q_{xy}$  is the in-plane wavevector transfer. (c) The cartoon illustrates the DPPC/FPTL LB monolayer, with the FPTL for the novel lipophilic  $C_{60}$ -derivative of three aliphatic chains attached to a fullerene cage.

monolayer of lipophilic  $C_{60}$ -derivative FPTL (6%) mixed with a phospholipid DPPC. From the data measured, we could extract the depth density profile and the in-plane characteristic structure for the monolayer of mixed lipids. Combining the reflectivity result with the temperature-dependent SAXS for the same mixed lipids but in the form of multilamellar vesicles in aqueous solutions (Figure 3), we obtained a better picture of the effect of the lipophilic- $C_{60}$ , when incorporated into the DPPC lipid membranes, on the bending and compression modulus of the host lipid membranes.<sup>5,6</sup>

In the study of DNA coated with a thin porous  $SiO_2$  layer in tetramethyl orthosilicate (TMOS) solutions for possible templates of silicate nanowires or nanotubes,<sup>7</sup> the silica-coated DNA wires prepared under a solution of 0.5 HCl were measured in solution using SAXS. The result revealed a coated-DNA wire-like structure of a rod-diameter of  $\sim 3$  nm (Figure 4(a)). To check the completeness of the silica coating layer of DNA, the silica-coated DNA solution was drop cast on mica substrate, and the thin cast film of silicated DNA wires was annealed at  $450^\circ C$  to burn out the DNA wire skeleton, leading to wire-type pores in the cured silica mold. The GISAXS technique with a synchrotron radiation source employed could detect the structure of the small amount of sample spread on the mica surface. The GISAXS

data measured for the cured silicated mold of DNA-pores reveal a similar wire-like pore structure with a shorter rod-length (Figure 4), compared to the silicated DNA rods before annealing. The result indicates that a thin silica layer could be coated relatively uniformly on DNA in the acid solution. Nevertheless, there were still defect spots without silica coating (protected), and these spots broke during the annealing, leading to a shorter length of the DNA-molded rod-like pores in the cured silica matrix.<sup>8</sup>

Very recently, the GISAXS at the NSRRC also develops further for an advanced study on a monolayer of InGaAs quantum dots as well as quantum wires. In Figure 5, the asymmetrical GISAXS pattern for a monolayer of  $In_{0.5}Ga_{0.5}As$  quantum dots revealed a skewed droplet shape for the dots. From the shoulder peak observed, the interparticle distance could also be deduced. With the incident energy scanned through the characteristic K-edge absorption of Ga, the composition and strain distribution inside the quantum dots could also be determined accurately from the energy dependent X-ray diffraction.<sup>9</sup>

### SAXS Activity at BL01B

In the past year, the SAXS activity at the NSRRC surged

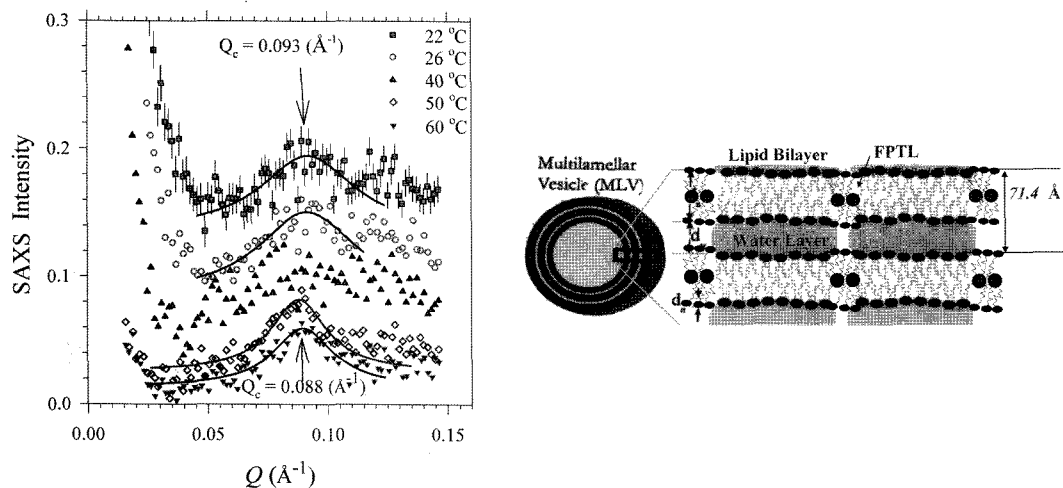


**Figure 3.** SAXS data for the FPTL-intercalated DPPC vesicles in water. The data are rescaled for clarity, and fitted (solid curves) with a Lorentzian function. The temperature-dependent evolution of the bilayers scattering peak of the DPPC/FPTL vesicles observed is reversible in the temperature range. The change in the peak positions during the temperature change narrates the history of FPTL's seizing control power on the host bilayers' structures and properties. The cartoon illustrates a possible structure inspired by the solution SAXS result.

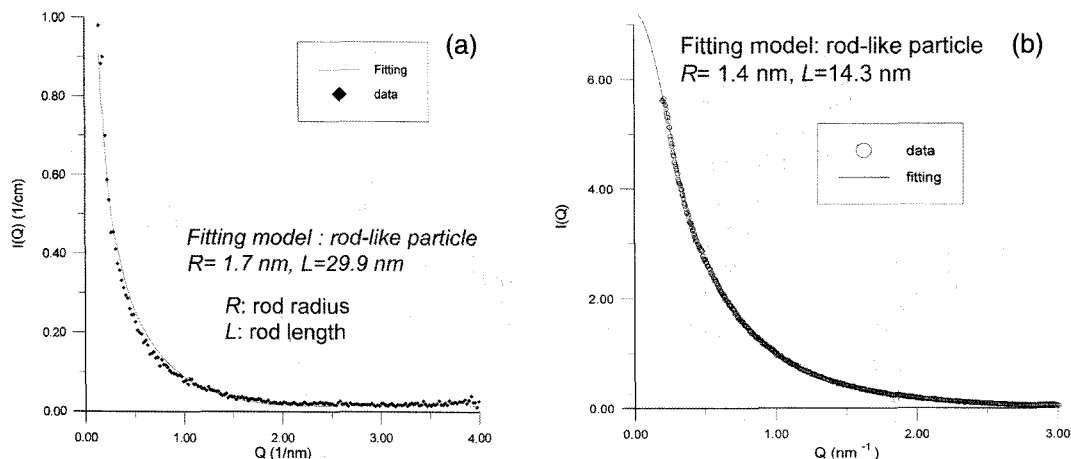


**Figure 4.** (a) SAXS data for the silicated-DNA in an aqueous solution of 0.5 M HCl. (b) GISAXS data for the cured silicated-DNA mold on mica after an annealing at 450 °C.

due to a new X-ray source generated by the superconducting wavelength shifter at the BL01B beamline of NSRRC. The new photon source can deliver a photon flux  $\sim 3 \times 10^{11}$  photons/s in the energy range of 5-23 KeV to the SAXS sample area. Before the installation of an unprecedented 30 nm resolution X-ray microscope to the beamline BL01B, we conducted several experiments to illustrate the merits of the advanced X-ray source, including temperature-dependent SAXS for the phase transitions of diblock polymers and copolymer/nanoparticle composites, time-dependent SAXS for the structural evolution of aluminum alloys under an artificial aging at high temperature, folding and unfolding of lysozyme in solutions, and anomalous small angle X-ray scattering (ASAXS) for studying the structure of Pt/Ru nanoparticles embedded in carbon grains for direct metha-

nol fuel cell (DMFC) applications, using photon energies near 11.5 and 22.1 KeV of the  $L_{III}$  and K absorption edges of Pt and Ru in ASAXS, respectively. Some of the results were reported previously.<sup>2</sup> Here we introduce the more recent developments in combing SAXS with other measurements, including simultaneous SAXS and wide-angle X-ray scattering (WAXS) measurements to monitor the correlation between mesoscale ordering and crystallization in a new class of self-assembled biomaterial, polypeptide-*block*-polypseudorotaxane diblock copolymer. We will also brief the simultaneous SAXS/DSC measurements for the morphology transformation of a PCL/PEG polymer blend.

Polymer structures in solutions or molten states are extremely soft, and easy to be manipulated by temperature or shearing force, for a controlled morphology. This type of

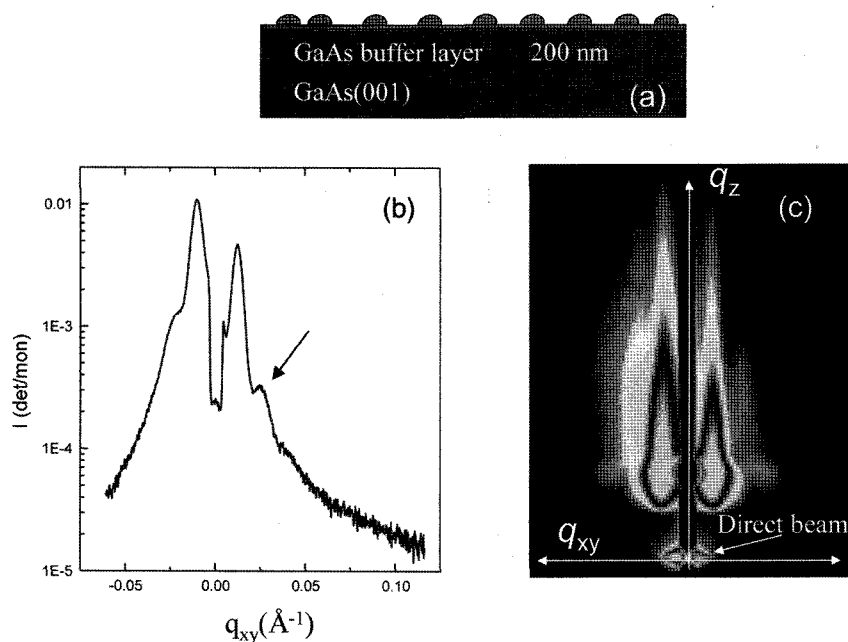


**Figure 5.** (a) A schematic for the uncapped  $\text{In}_{0.5}\text{Ga}_{0.5}\text{As}$  quantum dots. (b) The one-dimensional GISAXS profile with the interference peak indicated by an arrow. (c) The highly asymmetrical two-dimensional GISAXS pattern for the system.

study is important in identifying intermediate structures during phase transitions, or creating nanopatterns under the influence of processing procedure (solvent or external shear) for preferred structural characteristics that can be kinetically trapped or thermal equilibrium in the bulk states after cast from the controlled liquid or molten states. An example in this field of research at the NSRRC deals with the competition between liquid-liquid phase separation and crystallization in a polymer blend of poly( $\epsilon$ -caprolactone)/poly(ethylene glycol) (PCL/PEG). The simultaneous SAXS and DSC measurements (Figure 6) correlates the evolution of PCL crystallization (the onset of the exothermic trace of DSC) and the formation of long-range density fluctuations of PCL of a lamellar conformation (the broad peak at  $q \sim 0.045 \text{ \AA}^{-1}$  observed by SAXS), in the PCL/PEG system, when the temperature jump from  $160^\circ\text{C}$  of a homogeneous melt state to  $48^\circ\text{C}$  below the melting temperature ( $62^\circ\text{C}$ ) of PCL. The competition between phase separation and crystallization captured by synchronized SAXS/DSC and WAXS/DSC will be detailed in another report.<sup>10</sup>

With two linear position-sensitive detectors (20 cm in length) located respectively 110 and 30 cm behind the sample position, simultaneous SAXS/WAXS measurement has been explored at the NSRRC for the supramolecular self-assembly of a novel polypeptide-*block*-polypseudorotaxane. This diblock copolymer is comprised of an  $\alpha$ -helical polypeptide rod, based on  $\gamma$ -benzyl-L-glutamate, and an originally coiled segment  $\text{P}(\text{EO}_{19-r}\text{-}r\text{-PO}_3)$ , inclusion with  $\alpha$ -cyclodextrins ( $\alpha$ -CDs). Figure 7 shows the simultaneously appeared WAXS peak and SAXS peak for the diblock copolymer, when the

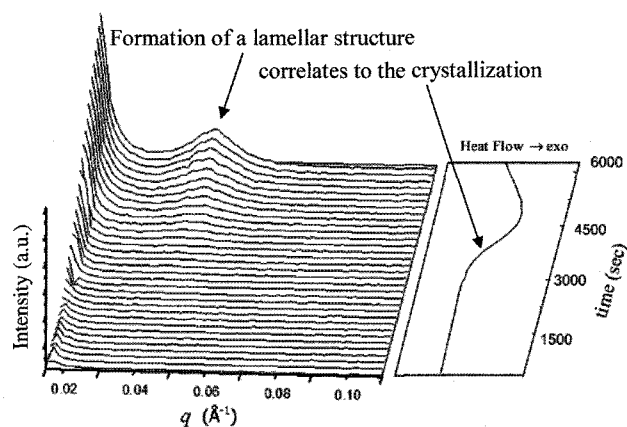


**Figure 6.** The time-dependent SAXS data (left) measured simultaneously with the DSC curve (right) for the structural evolution of a PCL/PEG polymer blend.

sample temperature ramped from  $30$  to  $100^\circ\text{C}$  for the liquid crystal transition temperature of the peptides. The result indicates that while the peptides formed a hexagonal packing in the liquid crystal transition (identified by WAXS separately),  $\alpha$ -CD was repelled out from the peptide phase and looped in the diblock copolymer for a channel-type crystallization (signified by the WAXS peak at  $q = 1.38 \text{ \AA}^{-1}$ ). Formation of the polypseudorotaxane converted the conformation of  $\text{P}(\text{EO}_{19-r}\text{-}r\text{-PO}_3)$  from a flexible chain into a rod-like structure, resulting in a novel block copolymer exhibiting a rod-rod conformation. In the meanwhile, the thus stiffened  $\alpha$ -CD- $\text{P}(\text{EO}_{19-r}\text{-}r\text{-PO}_3)$  rods formed another hexagonal packing

domains (identified by WAXS separately), and triggered a further hierarchical stacking with the peptide's hexagonal domains for the bilayer-like ordering (broad SAXS peak at  $q=0.025 \text{ \AA}^{-1}$ ), as illustrated in Figure 7. The SAXS/WAXS result revealed clearly the correlation between the formation of juxtaposed bilayer-like nanostructure with the formation of hexagonally packed PBLG stacks and channel-type

polypseudorotaxane moieties.<sup>11</sup>

In the last example, we would like to show a unique feature of using synchrotron X-ray for ASAXS at the NSRRC, in a structural study of Pt nanoparticles embedded in carbon matrix. The Pt/C system is considered as an effective catalytic electrode in the application of DMFC.<sup>12</sup> In Figure 8, the well-overlapped SAXS profiles in the low- $q$  region ( $q \lesssim$

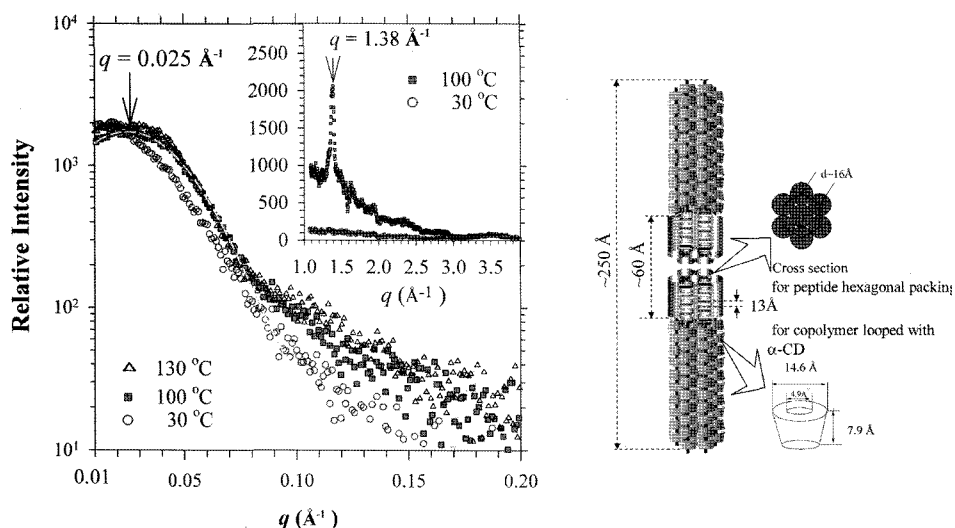


**Figure 7.** Simultaneous SAXS and WAXS (inset) data for the  $\alpha$ -CD- $P(\text{EO}_{19}\text{-}r\text{-PO}_3)\text{-}b\text{-PBLG}_{20}$  complex measured at 30, 100 and 130 °C. The peak at  $q=1.38 \text{ \AA}^{-1}$  (WAXS in the inset) observed at 100 and 130 °C, signifying the formation of channel crystallization of  $\alpha$ -CD. The cartoon illustrates the stacking of the two compatible hexagonal structures of the  $\alpha$ -CD-copolymer block and the peptide blocks in the complex, for a hexagonal-within-bilayer structure.

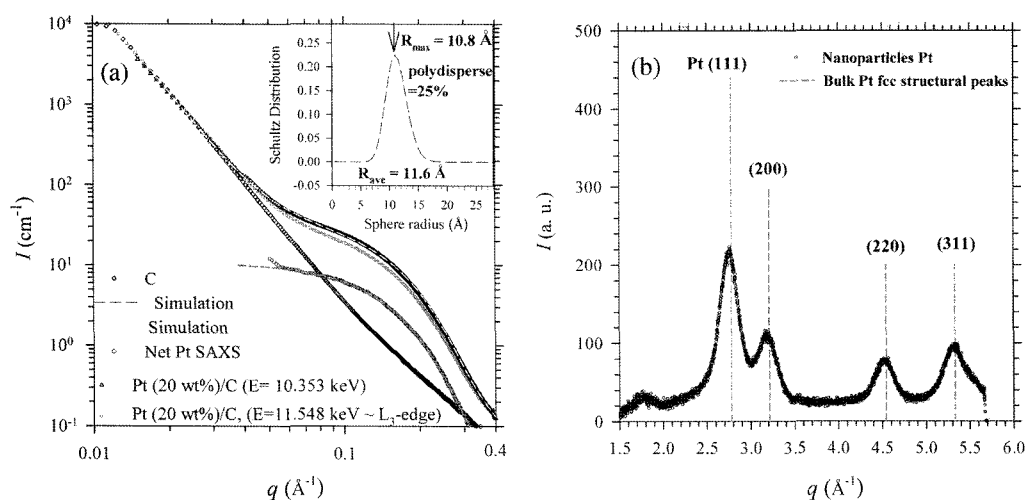


**Figure 8.** (a) SAXS and ASAXS data for the Pt nanoparticle embedded in carbon powders, measured at off-resonant and resonant energy, respectively. Also shown are the SAXS data for the carbon powder for comparison. The net scattering profile due to the ASAXS effect of the Pt nanoparticles is fitted using polydisperse spheres of a Schultz distribution (inset) characterized with a mean radius of  $R_{\text{ave}}=11.6 \text{ \AA}$  and a polydispersity of 25%. A simulation including the powder-law scattering contribution of the carbon powder and the scattering from Pt nanoparticles is also given for the SAXS data of Pt/C. (b) WAXS data exhibit the fcc cubic structural characteristics of the Pt nanoparticles. The lattice constant of  $3.935 \text{ \AA}$  extracted is slightly relaxed from the  $3.920 \text{ \AA}$  of the bulk Pt. The mean crystalline size estimated from the peak widths is  $22.7 \text{ \AA}$ , which is slightly smaller than the  $23.2 \text{ \AA}$  given by ASAXS for the over-all size, indicating a nanocrystalline structure for the Pt nanoparticles.

0.03 Å<sup>-1</sup>) for the pure carbon and Pt/C powders at two beam energies indicates that the carbon powder dominates the energy independent scattering in this region. With photon energy of the beam ( $E=11.548$  KeV) tuned near to the L<sub>3</sub> edge of Pt ( $E_{L3}=11.564$  KeV), the ASAXS profile measured shows an intensity drop from that measured at  $E=10.353$  KeV, in the intermediate to large- $q$  region ( $>0.1$  Å<sup>-1</sup>), where the Pt nanoparticles dominate the scattering. We can identify the structural characteristics of the resonant atoms Pt from the differences in the SAXS and ASAXS profiles induced by the anomalous scattering characteristics, as explained by Haubold *et al.*<sup>13</sup> Here, the pure ASAXS effect from the Pt nanoparticle is extracted using  $I(q)_{\text{Pt-ASAXS}}=I(q,E=10.352 \text{ KeV})-I(q,E=11.548 \text{ KeV})$ , to eliminate the energy independent scattering contribution from the carbon powder. We further fit the profile  $I(q)_{\text{Pt-ASAXS}}$  using a model of polydisperse spheres with a Schultz distribution, as shown in the inset of Figure 8, and obtained a fitted mean radius of  $11.6 \pm 0.3$  Å, and a polydispersity of ~25% for the Pt nanoparticles in fine carbon powder. The structural information deduced from ASAXS combined with the WAXS data measured (Figure 8) for crystalline properties illustrates a better structural picture for the Pt nanoparticles.

### A Dedicated SAXS Beamline Planned at NSRRC

On the basis of the active science projects and the broad interests of the NSRRC SAXS users, NSRRC has launched a SAXS research program for soft matter and nanostructures, including the installation of a dedicated SAXS beamline to a new In-Achromate superconducting wiggler (IASW) X-ray source, of  $\sim 10^{12}$ - $10^{13}$  photons/s in the energy range of 5-23 KeV. The planned SAXS beamline will be featured in four operation modes, including (1) high  $q$ -resolution mode, (2) high flux mode, (3) ASAXS mode, and (4) GISAXS mode.

**High  $q$ -Resolution Mode.** In the high  $q$ -resolution mode, the measurable minimum  $q$  value is targeted to be  $0.002$  Å<sup>-1</sup> with  $\pm 10\%$  uncertainty, which translates into a maximum resolvable lamellar spacing of 300 nm (using the Bragg law). A detailed estimation shows that to have a measurable  $q$ -minimum at  $0.002$  Å<sup>-1</sup> with  $\pm 10\%$  uncertainty, we need to have a 0.5 mm dia. beam (8 KeV photons assumed) with a small beam divergence of  $\Delta\theta=\pm 50$   $\mu\text{rad}$  at the detector position, together with a sample-to-detector distance of 5 m and a detector pixel resolution of 200  $\mu\text{m}$ .

**High Flux Mode.** We target a flux of  $\sim 2 \times 10^{12}$  photon/s at the sample area in the high flux mode designed mainly for time-resolved experiments of a sub-millisecond time resolution. This time resolution is needed in studying the middle to late stage folding dynamics of biomolecules (proteins) in solutions or other fast dynamic phase transitions. Roughly, to have  $\sim 10^5$  photons in each data frame of 100 data channels for enough data statistics, with a data collection time of

0.1 ms (minimum-resolved time interval) for typical biomolecule solutions of a scattering efficiency of  $\sim 5 \times 10^{-4}$ , we need  $\sim 2 \times 10^{12}$  photon/s. In the high flux mode, a double-multilayer monochromator (DMM) with  $\Delta\lambda/\lambda \sim 0.01$  can provide an intensity  $\sim 20$ -50 times more than that by the DCM of  $\Delta\lambda/\lambda \sim 2 \times 10^{-4}$  used in the high- $q$  resolution mode.

**ASAXS Mode.** The wide energy range 5-23 KeV provided by the IASW photon source will grant the capability of performing ASAXS for most of the atoms in the periodic table using either K- or L<sub>III</sub>-absorption edges, with the exception of the atoms of atomic numbers lower than 23 of Vanadium and atomic numbers between 45 (Rh) and 54 (Xe). An energy resolution  $<10$  eV, or  $\Delta E/E \approx 5 \times 10^{-4}$  for the incident beam of the ASAXS measurement is required for a better ASAXS effect. This energy resolution allows, generally,  $\sim 10\%$  resolution in resolving the composition in a system of multi-elements (phases).

**GISAXS Mode.** The critical angle of thin film samples for total X-ray reflection is an important reference in setting the incident angle for GISAXS measurements. A proper beam incident angle with a typical accuracy better than  $0.005^\circ$  can effectively keep the incident beam inside a thin sample film, leading to a better sample scattering volume and a less background scattering from the sample substrate. It will be advantageous to equip the SAXS endstation with the capability of reflectivity scan to determine the critical angle of sample thin films.

### Summary

We have described the recent SAXS activity at the NSRRC, including GISAXS, solution SAXS, ASAXS, SAXS/WAXS, and SAXS/DSC. We have also introduced a dedicated SAXS beamline planned for expanding the current SAXS activity and scope at the NSRRC, especially in time-resolved SAXS and ASAXS for soft matter and nanoscience.

**Acknowledgements.** We thank H.-F. Lee, H.-L. Shei, J.-M. Lin, Dr. J.-F. Lee for providing samples and/or results for this review.

### References

- (1) O. Glatter and O. Kratky, *Small Angle X-ray Scattering*, Academic Press INC., London, New York, 1980.
- (2) Y. H. Lai, Y. S. Sun, U. Jeng, Y. F. Song, K. L. Tsang, and K. S. Liang, *Nucl. Inst. Meth. Phys. Res. B*, **238**, 205 (2005).
- (3) C.-H. Hsu, H.-Y. Lee, K. S. Liang, U. Jeng, D. Windover, T. M. Lu, and C. Jin, *Mat. Res. Soc. Symp. Proc.*, **612**, D5.23.1 (2002).
- (4) C.-H. Hsu, U. Jeng, H.-Y. Lee, D. Windover, T.-M. Lu, and C. Jin, *Thin Solid Films*, **472/1-2**, 323 (2004).
- (5) U. Jeng, C.-H. Hsu, T.-L. Lin, C.-M. Wu, H.-L. Chen, L.-A.

- Tai, and K.-C. Hwang, *Physica B*, **357**, 193 (2005).
- (6) U. Jeng, T.-L. Lin, K. Shin, C.-H. Hsu, H.-Y. Lee, M. H. Wu, Z. A. Chi, M. C. Shih, and L. Y. Chiang, *Physica B*, **336**, 204 (2003).
- (7) J. Richter, R. Seidel, R. Kirsch, M. Mertig, W. Pompe, J. Plaschke, and H. K. Schackert, *Adv. Mater.*, **12**, 507 (2000).
- (8) T.-L. Lin, H.-L. Hsieh, J.-M. Lin, U. Jeng, C.-H. Hsu, and W. Liou, in preparation.
- (9) C. H. Hsu *et al.*, in preparation.
- (10) W.-T. Chuang, U. Jeng, H.-S. Sheu, and P.-D. Hong, accepted *Macromol. Res.*.
- (11) H.-F. Lee, H.-S. Sheu, U. Jeng, C.-F. Huang, and F.-C. Chang, *Macromolecules*, **38**, 6551 (2005).
- (12) C.-S. Tsao, H.-L. Chang, U. Jeng, J.-M. Lin, and T.-L. Lin, *Polymer*, **46/19**, 8430 (2005).
- (13) H.-G. Haubold, X. H. Wang, G. Goerigk, and W. Schilling, *J. Appl. Cryst.*, **30**, 653 (1997).